International Journal of Heat and Mass Transfer 162 (2020) 120365

Contents lists available at ScienceDirect

International Journal of Heat and Mass Transfer

journal homepage: www.elsevier.com/locate/hmt

A ghost-cell discrete unified gas kinetic scheme for thermal flows with heat flux at curved interface

Shi Tao*, Qing He*, Baiman Chen, Frank G.F. Qin, Yousheng Lin

Guangdong Provincial Key Laboratory of Distributed Energy Systems, Dongguan University of Technology, Dongguan 523808, China

ARTICLE INFO

Article history:
Received 16 March 2020
Revised 15 August 2020
Accepted 18 August 2020
Available online 26 August 2020

Keywords:
DUGKS
Ghost-cell method
Heat-flux boundary condition
Convection-diffusion
Curved interface

ABSTRACT

The discrete unified gas kinetic scheme (DUGKS) is advanced for simulating thermal convections with curved heat flux condition using the ghost-cell (GC) approach. The fluid flow and temperature field combined under the Boussinesq approximation are solved by the double-population model. The ghost-cell immersed boundary method is applied to the curved heat-flux interface, where fictitious cells are set in the solid domain. The information at the centers of those cells is extrapolated from the fluid-solid interface and the neighboring flow. The heat-flux boundary condition at the interface can then be incorporated into the solution of the entire thermal flow. Note that the extrapolation/interpolation involved in the GC-DUGKS is accomplished through a sharp interface manner. Therefore, the difficulty in handling the heat-flux boundary condition for the diffuse-type immersed boundary methods due to the cross contamination is removed. Furthermore, the thermal buoyancy force is conveniently combined with the governing equation by the Strang-splitting scheme. Simulations of several well-established convection-diffusion flow problems with heat flux at the curved interface are performed to validate the present GC-DUGKS. The results demonstrate the accuracy and feasibility of the method.

© 2020 Elsevier Ltd. All rights reserved.

1. Introduction

Thermal flows with complex geometry are widely encountered in the energy, environment and chemical fields, such as the heat transfer through heat exchanger, diffusion of pollutants in the porous media and drying processes in the fluidized bed [1,2]. Those flows are generally subjected to the Navier-Stokes and convection-diffusion (NS-CD) equations, coupled with a suitable boundary condition for the fluid-solid interface. The finite difference and element methods, as the representative of traditional computational fluid dynamics (CFD) are previously applied to the solution of the NS-CD equations. On the other hand, the kinetic scheme, taking the lattice Boltzmann method (LBM), lattice Boltzmann flux solver (LBFS) and discrete unified gas kinetic scheme (DUGKS) for example, has received an increasing concern in the recent years. Those methods are derived from the Boltzmann equation which connects the macroscopic hydrodynamics with the microscopic physics. They fall into the mesoscopic approach and are generally considered to have some advantages over the conventional CFD methods. For example, the pressure can be directly evaluated from the equation of state, rather than solving the time-consuming Possion equation; furthermore, the advection term in the NS equations has strong nonlinearity, while the counterpart is linear in the Boltzmann equation.

Successful applications by the lattice Boltzmann method have been conducted in the literature [3–6]. The LBM applies a finite-difference discretization to the Boltzmann model equations. Fictitious particles are assumed to continuously execute two steps of collision and streaming. Since constrained within uniform lattices, the particles can only move along several directions, for instance, nine velocities for the two-dimensional flow (called D2Q9 model) [5]. Those features facilitate the simple program framework and easy implementation of LBM, and eventually render excellent parallel performance which is important for large-scale computing [54]. However, it still faces some difficulties for low convergence rate of steady flow, inflexibility meshes, and cumbersome in compressible flow [6].

In view of this, various improved schemes have been developed [7–10]. Particularly, the DUGKS adopted in the present study is recently proposed by Guo et al. [9,10], which solves the Boltzmann model equations in a finite volume formulation. The most distinguished feature of DUGKS lies in the use of discrete characteristic solutions of the Boltzmann equation for evaluating the micro-flux across the cell interface. That procedure contributes to a simple mathematical form for combining the effects of free migration and collision of the fictitious particles. The temporal step size in DUGKS is not limited by the mean collision time of particles, and the spa-

* Corresponding authors.
E-mail addresses: taoshi@dgut.edu.cn (S. Tao), heqing@dgut.edu.cn (Q. He).

https://doi.org/10.1016/j.ijheatmasstransfer.2020.120365
0017-9310/© 2020 Elsevier Ltd. All rights reserved.

tial step size no longer has to be smaller than the mean free path. Therefore, the DUGKS is capable of simulating all Knudsen number flows [11-13]. Particularly, for the continuum flows, the comparative studies conducted by Wang et al. [43,44] and Zhu et al. [45] all demonstrated that the DUGKS had some advantages of stability and accuracy over LBM. Most recently, this method has been successfully applied to thermal flows [14,15]. It is worth noting that another powerful flow solver which largely overcomes the limitation of LBM is the lattice Boltzmann flux solver (LBFS) [46]. The LBFS also has a finite volume formulation, and more especially, the interface flux is evaluated efficiently by the local solution of the so-called lattice Boltzmann equation. Since first developed by Shu and his coworkers [46,47], the extension and application of LBFS has also been greatly advanced in recent years [48].

On the other hand, suitable boundary scheme should be specified in the simulation of thermal flows. The immersed boundary (IB) method is considered to be a promising approach for flows with complex geometry, because of decoupling the solution of governing equation and the enforcement of boundary condition. The IB method first proposed by Peskin et al. [16] is generally implemented within the Cartesian grid system, using simple non-body-conformal meshes. In the IB method, the Lagrangian markers are evenly distributed along the boundary, which produce the external force and heat source/sink. Those terms will be added in the governing equations, and impact both sides of the interface. Eventually, the boundary is smeared in several meshes. Such diffuse property may induce some unphysical phenomena in the simulation of flows with the isothermal wall, i.e., streamline penetration into the interface and significant inconsistency between the computed and desired temperatures [17,18]. The diffusion of the interface can be alleviated through the adoption of the modified explicit-forcing [19], implicit-forcing [20], multi-forcing [21] and interface-thickening [22] methods. Improved simulation results for the flow with isothermal wall have been reported in the literature [23,24]. However, some recent studies found that those corrected methods cannot be directly extended to the thermal flows with heat-flux interface [25,26].

Another type of IB method is the sharp interface scheme, which includes the ghost-cell (GC) approach adopted in this study. In the GC scheme [27], for the purpose of extending the flow solution to the solid domain, the solid cell that has at least one link intersected by the interface is transformed deliberately to be a fluid cell. The information at such cell is then extrapolated from the interface and the neighboring flow. Compared with the diffuse-type IB method [16], there is no need to introduce the body force into the governing equation; furthermore, the interface is distinguishable, which contributes to the easy enforcement of the heat flux condition. The main objective of this paper is to extend the DUGKS for the thermal convections with curved heat flux condition by combining the GC method. The remaining part of this work is organized as follows. Section 2 is devoted to introducing the combination of DUGKS and GC method. The method is validated in Section 3. Finally, a summary is presented in Section 4.

2. Numerical method

2.1. DUGKS for thermal flow

The viscous flow with heat transfer considered in this study is incompressible, which can be described by the NS-CD equations,

$$\nabla.\boldsymbol{u} = 0, \tag{1}$$

$$\frac{\partial \boldsymbol{u}}{\partial t} + \boldsymbol{u}.\nabla\boldsymbol{u} = -\frac{1}{\rho}\nabla p + \nu\nabla^2\boldsymbol{u} + \boldsymbol{a}_g, \tag{2}$$

$$\frac{\partial T}{\partial t} + \nabla.(\boldsymbol{u}T) = \kappa\nabla^2 T, \tag{3}$$

where the $\boldsymbol{u}$, ρ, p, and T are respectively the flow parameters of velocity, density, pressure and temperature. The viscosity ν and thermal diffusivity κ are both the parameters of fluid physical property. The thermal buoyancy $\boldsymbol{a}_g$ is a function of the gravity acceleration g_0, thermal expansion coefficient β and temperature difference, and can be expressed under the Boussinesq approximation [28] as

$$\boldsymbol{a}_g = g_0\beta(T - T_0)\boldsymbol{j}. \tag{4}$$

where T_0 denotes the average fluid temperature.

For the solution of the above-mentioned NS-CD equations, the double-population model of DUGKS is implemented as [29]

$$\frac{\partial f}{\partial t} + \boldsymbol{\xi}.\nabla f = \frac{f^{eq} - f}{\tau_f} + F_g, \quad \frac{\partial g}{\partial t} + \boldsymbol{\xi}.\nabla g = \frac{g^{eq} - g}{\tau_T}. \tag{5}$$

In Eq. (5), f and g are the distribution functions for the fluid flow and temperature field, which both denote the probability to find a particle with velocity $\boldsymbol{\xi}$ at position $\boldsymbol{x}$ and time t. τ_f and τ_T are the relaxation times in the Bhatnagar, Gross and Krook (BGK) collision operator. f^{eq} and g^{eq} are the Maxwellian-type equilibrium distribution functions [9] as

$$f^{eq} = \frac{\rho}{2\pi RT_1}\exp\left(-\frac{(\boldsymbol{\xi} - \boldsymbol{u})^2}{2RT_1}\right), \quad g^{eq} = \frac{T}{2\pi RT_1}\exp\left(-\frac{(\boldsymbol{\xi} - \boldsymbol{u})^2}{2RT_1}\right), \tag{6}$$

where $RT_1 = c_s^2$ is the artificial sound speed. F_g is the force term in the DUGKS [2,13] as

$$F_g = -\boldsymbol{a}_g.\nabla_\xi f \approx -\boldsymbol{a}_g.\nabla_\xi f^{eq} = \boldsymbol{a}_g.\frac{(\boldsymbol{\xi} - \boldsymbol{u})}{RT_1}f^{eq}, \tag{7}$$

As a kinetic scheme, the ρ, $\boldsymbol{u}$ and T are considered to be the conservative flow variables in DUGKS, which are defined by the moments of the distribution function as

$$\rho = \int f d\boldsymbol{\xi}, \quad \rho\boldsymbol{u} = \int \boldsymbol{\xi} f d\boldsymbol{\xi} + \frac{1}{2}\Delta t\rho\boldsymbol{a}_g, \quad T = \int g d\boldsymbol{\xi}. \tag{8}$$

Note that the body force also affects the velocity, which has been taken into account in Eq. (8).

2.1.1. Strang-Splitting method for force incorporation

The body force term involved in the double-population model of Eq. (5) should be first handled in the application of DUGKS. For such purpose, the Strang-Splitting method [30] is used in the present study. In that scheme, the force is divided into two equal parts, which respectively impact on the distribution function through the pre-forcing and post-forcing procedures as

$$\frac{\partial f}{\partial t} = \frac{1}{2}F_g, \tag{9}$$

$$\frac{\partial f}{\partial t} + \boldsymbol{\xi}.\nabla f = \Omega_f = \frac{f^{eq} - f}{\tau_f}, \quad \frac{\partial g}{\partial t} + \boldsymbol{\xi}.\nabla g = \Omega_T = \frac{g^{eq} - g}{\tau_T}, \tag{10}$$

$$\frac{\partial f}{\partial t} = \frac{1}{2}F_g. \tag{11}$$

In the two forcing steps given by Eqs. (9) and (11), both the distribution function and the velocity should be updated as

$$f^* = f + 0.5\Delta t F_g, \tag{12}$$

$$\boldsymbol{u}^* = \boldsymbol{u} + 0.5\Delta t\boldsymbol{a}_g, \tag{13}$$

Eq. (10) is the pure DUGKS process, which is to be introduced subsequently.

2.1.2. DUGKS without external force

The DUGKS for updating the fluid distribution function f according to the Boltzmann Eq. (10) is explained in this subsection. The temperature counterpart can be constructed similarly. After applying the midpoint rule and the trapezoidal scheme respectively to the convection and collision terms, the Eq. (10) is discretized by DUGKS as [9,13]

$$f_j^{n+1} - f_j^n + \frac{\Delta t}{|V_j|} F^{n+1/2} = \frac{\Delta t}{2}\left(\Omega_j^{n+1} + \Omega_j^n\right). \tag{14}$$

Here, Δt is the time step. $F^{n+1/2}$ expressed as

$$F^{n+1/2} = \int_{\partial V_j} \left(\boldsymbol{\xi}.\boldsymbol{n}\right) f(\boldsymbol{x}, t_{n+1/2}) d\boldsymbol{S}, \tag{15}$$

denotes the microscopic flux across the surface ∂V_j of the control volume V_j, with $\boldsymbol{n}$ the outward unit vector normal to the interface. Note that both values of f_j^n and Ω_j^n are averaged in the volume $|V_j|$. Note that f_j cannot be explicitly updated through the Eq. (14) due to the existence of the collision term Ω_j^{n+1}. That implicity can be removed by introducing two auxiliary distribution functions,

$$\tilde{f} = f - \frac{\Delta t}{2}\Omega, \qquad \tilde{f}^+ = f + \frac{\Delta t}{2}\Omega. \tag{16}$$

Eq. (14) is converted to be as

$$\tilde{f}_j^{n+1} = \tilde{f}_j^{+,n} - \frac{\Delta t}{|V_j|} F^{n+1/2}. \tag{17}$$

It is clear that $\tilde{f}^+$ can be derived from $\tilde{f}$ and the equilibrium distribution function as

$$\tilde{f}^+ = \frac{2\tau - \Delta t}{2\tau + \Delta t}\tilde{f} + \frac{2\Delta t}{2\tau + \Delta t} f^{eq}. \tag{18}$$

Particularly, $\tilde{f}$ is actually updated in the simulation since we can evaluate the macroscopic quantities directly from $\tilde{f}$ according to Eq. (8).

The remaining task is to identify the flux $F^{n+1/2}$ for updating the $\tilde{f}$, which is a function of $f(\boldsymbol{x}_b, t_{n+1/2})$ with $\boldsymbol{x}_b$ the center of a cell interface and $t_{n+1/2} = (t_n + \Delta t/2)$. Therefore, the governing Eq. (10) is integrated along the characteristic line from time t_n to $t_{n+1/2}$,

$$\begin{aligned} &f(\boldsymbol{x}_b, \boldsymbol{\xi}, t_n + h) - f(\boldsymbol{x}_b - \boldsymbol{\xi}h, \boldsymbol{\xi}, t_n) \\ &= \frac{h}{2}\left[\Omega(\boldsymbol{x}_b, \boldsymbol{\xi}, t_n + h) + \Omega(\boldsymbol{x}_b - \boldsymbol{\xi}h, \boldsymbol{\xi}, t_n)\right], \end{aligned} \tag{19}$$

where the trapezoidal rule is again applied to Ω, and $h = \Delta t/2$. Eq. (19) is implicit, and similarly, another set of new distribution functions are introduced here,

$$\bar{f} = f - \frac{h}{2}\Omega, \qquad \bar{f}^+ = f + \frac{h}{2}\Omega, \tag{20}$$

with

$$\bar{f}^+ = \frac{2\tau - h}{2\tau + h}\bar{f} + \frac{2h}{2\tau + h} f^{eq}. \tag{21}$$

Then we obtain

$$\bar{f}(\boldsymbol{x}_b, \boldsymbol{\xi}, t_n + h) = \bar{f}^+(\boldsymbol{x}_b - \boldsymbol{\xi}h, \boldsymbol{\xi}, t_n). \tag{22}$$

Eq. (22) can be rewritten as

$$\bar{f}(\boldsymbol{x}_b, \boldsymbol{\xi}, t_n + h) = \bar{f}^+(\boldsymbol{x}_b, \boldsymbol{\xi}, t_n) - \boldsymbol{\xi}h.\nabla\bar{f}^+(\boldsymbol{x}_b, \boldsymbol{\xi}, t_n). \tag{23}$$

With the Eq. (23) at hand, the interface distribution function that we need is then identified,

$$f(\boldsymbol{x}_b, \boldsymbol{\xi}, t_n + h) = \frac{2\tau}{2\tau + h}\bar{f}(\boldsymbol{x}_b, \boldsymbol{\xi}, t_n + h) + \frac{h}{2\tau + h} f^{eq}(\boldsymbol{x}_b, \boldsymbol{\xi}, t_n + h), \tag{24}$$

where the macroscopic quantities are evaluated from $\bar{f}(\boldsymbol{x}_b, \boldsymbol{\xi}, t_n + h)$ according to Eq. (8). The flux $F^{n+1/2}$ is then determined according to Eq. (15), and finally, $\tilde{f}$ is updated by Eq. (17). Particularly, $\bar{f}^+$ and $\tilde{f}^+$ can be efficiently computed as

$$\bar{f}^+ = \frac{2\tau - h}{2\tau + \Delta t}\tilde{f} + \frac{3h}{2\tau + t} f^{eq}, \tag{25}$$

$$\tilde{f}^+ = \frac{4}{3}\bar{f}^+ - \frac{1}{3}\tilde{f}. \tag{26}$$

The temporal and spatial discretization of the BGK-type Boltzmann Eq. (10) is completed by now. We have to further discretize the velocity space in the implementation of DUGKS. The 1D discrete particle velocities and the corresponding weights can be determined by the three-point Gauss-Hermite quadrature [9,31] as $\xi_i = \sqrt{3}c_s[-1,\ 0,\ 1]$ and $W_2 = 2/3$, $W_1 = W_3 = 1/3$, respectively. For the 2D problems considered in this study, the velocity and weights can be derived by the tensor product method as

$$\begin{aligned} &\boldsymbol{\xi}_i = \sqrt{3}c_s\begin{bmatrix} -1 & -1 & -1 & 0 & 0 & 0 & 1 & 1 & 1 \\ -1 & 0 & 1 & -1 & 0 & 1 & -1 & 0 & 1 \end{bmatrix}, \\ &W_i = \begin{cases} \frac{4}{9}, & i = 5 \\ \frac{1}{9}, & i = 2, 4, 6, 8 \\ \frac{1}{36}, & i = 1, 3, 7, 9. \end{cases} \end{aligned} \tag{27}$$

For low speed flows, i.e., the Mach number defined as $Ma = |\boldsymbol{u}|/c_s = |\boldsymbol{u}|/\sqrt{RT_1}$ is much less than 1.0, the equilibrium distribution function can be simplified with the second-order term of Ma involved as

$$f_i^{eq} = W_i\rho\left[1 + \frac{\boldsymbol{\xi}_i.\boldsymbol{u}}{RT_1} + \frac{\left(\boldsymbol{\xi}_i.\boldsymbol{u}\right)^2}{2(RT_1)^2} - \frac{|\boldsymbol{u}|^2}{2RT_1}\right]. \tag{28}$$

The flow parameters and the physical properties of the fluid can be evaluated as

$$\begin{aligned} &\rho = \sum_i f_i, \quad \rho\boldsymbol{u} = \sum_i \boldsymbol{\xi}_i f_i, \quad p = \rho RT_1, \quad \nu = \tau_f RT_1, \\ &T = \sum_i g_i, \quad \kappa = \tau_T RT_1, \end{aligned} \tag{29}$$

2.1.3. Boundary scheme for straight interface

As a kinetic scheme, the boundary treatment in the DUGKS is to identify the unknown distribution function (UDF), where its velocity satisfies $\boldsymbol{\xi}_i.\boldsymbol{n} > 0$ with $\boldsymbol{n}$ the outward unit vector normal to the surface. Specifically, since we usually locate the straight surface along the cell interface, the interface distribution functions $\bar{f}$ and $\bar{g}$ pointing to the fluid and temperature fields should be evaluated. The bounce-back (BB) scheme [29,32] mimics a scenario that a particle hitting the wall just reverses the direction as

$$\bar{f}\left(\boldsymbol{x}_w, \boldsymbol{\xi}_i, t + h\right) = \bar{f}\left(\boldsymbol{x}_w, -\boldsymbol{\xi}_i, t + h\right) + 2\rho_w W_i \frac{\boldsymbol{\xi}_i.\boldsymbol{u}_w}{RT_1}. \tag{30}$$

Here, $\boldsymbol{u}_w$ and ρ_w are the interface velocity and density, which are given by the physical condition and its definition, respectively. We can also set ρ_w to be the average fluid density in the simulation of incompressible flow. It is clear that the BB rule in Eq. (30) renders the no-slip boundary condition. For the thermal flow, the surface can be insulated, or has predefined temperature, where the UDFs at the interface are expressed respectively as [33]

$$\bar{g}\left(\boldsymbol{x}_w, \boldsymbol{\xi}_i, t + h\right) = \bar{g}\left(\boldsymbol{x}_w, -\boldsymbol{\xi}_i, t + h\right), \tag{31}$$

$$\bar{g}\left(\boldsymbol{x}_w, \boldsymbol{\xi}_i, t + h\right) = -\bar{g}\left(\boldsymbol{x}_w, -\boldsymbol{\xi}_i, t + h\right) + 2W_i T_w. \tag{32}$$

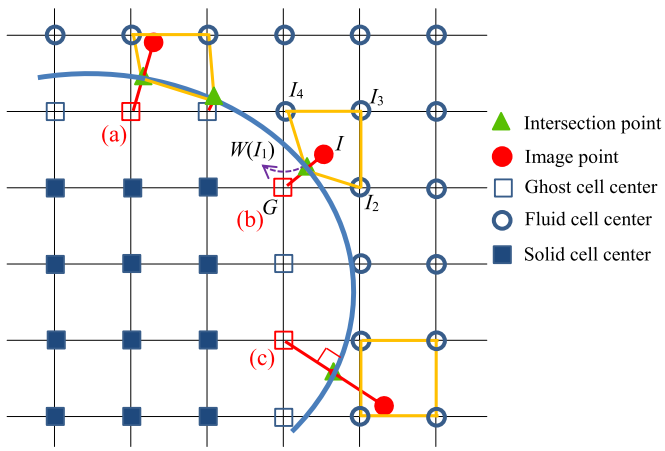

Fig. 1. Geometry configuration and the interpolation stencils in the present ghost-cell method. Point G is the center of a ghost cell, which is located in the solid zone and concurrently has at least one link intersected by the fluid-solid interface. W is on the interface and nearest to G. I is a corresponding image point in the fluid domain, which is in mirror symmetry with G regarding the interface, i.e., $||GW|| = ||IW|| = l$. I_1 ~ I_4 are the four neighboring nodes within the interpolation stencil of I. The neighboring points can all be the fluid cell center (case (c)), or a combination of the fluid cell center and intersection point (cases (a) and (b)).

2.2. Ghost-cell method for curved interface

The boundary conditions at the straight interface can be conveniently implemented by the BB-type rules in the DUGKS. However, it is a non-trivial task to handle the curved boundaries using Cartesian mesh. The ghost-cell (GC) method is applied for such purpose in this study, where the first procedure is to classify the cell status. A general configuration is delineated in Fig. 1. The fluid and solid cells are the center of the computation meshes located at the fluid and solid domains, respectively. The solid cell which center has at least one link intersected by the interface are further transformed to be the ghost cell. The information at that cell is unknown, which is to be evaluated from the interface and the neighboring flow. The direction of the local external normal vector is identified and applied for extrapolation.

Taking point G in Fig. 1 for example, it is the center of a ghost cell, and W and I are the corresponding intersection and image nodes. Note that point I is in mirror symmetry of G regarding the interface at W, i.e., $||GW|| = ||IW|| = l$. The fluid and temperature distribution functions (both denoted by $\tilde{\phi}$) at G is concerned in the boundary treatment. They can be constructed using the non-equilibrium extrapolation [55], or directly distribution function extrapolation [56,57]. As demonstrated by Guo et al. [5,55], the former generally has better numerical stability than the latter. Therefore, the method of non-equilibrium extrapolation is adopted in this study, where the distribution function is expressed as the combination of the equilibrium and non-equilibrium portions,

$$\tilde{\phi}\left(\boldsymbol{x}_G, \boldsymbol{\xi}_i, t\right) = \phi^{eq}\left(\boldsymbol{x}_G, \boldsymbol{\xi}_i, t\right) + \phi^{neq}\left(\boldsymbol{x}_G, \boldsymbol{\xi}_i, t\right), \tag{33}$$

According to the Eq. (28), the equilibrium part is directly obtained from the macroscopic quantities of the density, temperature and velocity (all denoted by ψ) as $\phi^{eq}(\boldsymbol{x}_G) = \phi^{eq}(\psi(\boldsymbol{x}_G))$. As outlined previously, the $\psi(\boldsymbol{x}_G)$ and $\phi^{neq}(\boldsymbol{x}_G)$ are to be extrapolated from the interface and the neighboring flow. There are three kinds of boundary treatment for the ψ involved in the present study, i.e., the Dirichlet, Neumann, and Robin conditions. For the former, the value of ψ is known constant at the intersection node W, i.e., $\psi(\boldsymbol{x}_W) = C$, and a second-order extrapolation can be applied,

$$\psi(\boldsymbol{x}_G) = 2\psi(\boldsymbol{x}_W) - \psi(\boldsymbol{x}_I). \tag{34}$$

The Neumann condition is a normal gradient condition, where the $\psi(\boldsymbol{x}_G)$ can be obtained as

$$\psi(\boldsymbol{x}_G) = \psi(\boldsymbol{x}_I) - 2l\frac{\partial\psi(\boldsymbol{x}_W)}{\partial\boldsymbol{n}}. \tag{35}$$

The third is a combination of the Dirichlet and Neumann conditions as $m_1\psi(\boldsymbol{x}_W)/\boldsymbol{n} + m_2\psi(\boldsymbol{x}_W) = m_3$, where the m_1, m_2 and m_3 are three constant parameters involved. Here, the $\psi(\boldsymbol{x}_G)$ is evaluated as

$$\psi(\boldsymbol{x}_G) = \frac{2m_3 l - (m_1 + m_2 l)\psi(\boldsymbol{x}_I)}{m_2 l - m_1}. \tag{36}$$

The density is generally assumed to subject to the Neumann condition with zero normal gradient [41,42,53], i.e., $\rho(\boldsymbol{x}_W)/\boldsymbol{n} = 0$, which has

$$\rho(\boldsymbol{x}_G) = \rho(\boldsymbol{x}_I). \tag{37}$$

The non-equilibrium part can be determined analogically with $\phi^{neq}(\boldsymbol{x}_W)/\boldsymbol{n} = 0$,

$$\phi^{neq}(\boldsymbol{x}_G) = \phi^{neq}(\boldsymbol{x}_I). \tag{38}$$

The above Eqs. (36) and (37) are given according to the symmetric reflection method (i.e., first-order extrapolation) [51], which is usually combined with Eqs. (34) and (35) to exert the non-penetration condition on the interface. Note that a high-order extrapolation with two and more points involved can also be adopted for such purpose, where a non-zero normal gradient exists in those methods [51,52,42]. The symmetric reflection method adopted here is capable of simulating the low-speed incompressible flow considered in this study [27].

The remaining is to identify the macroscopic quantities and non-equilibrium distribution function at the image point I, i.e., $\psi(\boldsymbol{x}_I)$ and $\phi^{neq}(\boldsymbol{x}_I)$ (both denoted by $(\boldsymbol{x}_I)$). A generalized bilinear interpolation (GBI) scheme [34] is adopted here,

$$\chi(\boldsymbol{x}) = ax + by + cxy + d, \tag{39}$$

with $\boldsymbol{x} = (x, y)$. In the above Eq. (39), the four parameters a, b, c and d involved are to be evaluated by the four points from I_1 to I_4 surrounding the $\boldsymbol{x}_I$. That is to say, the GBI is also applicable to those neighboring nodes, and the a, b, c and d can then be identified through the root-finding. As shown in Fig. 1, the four neighboring points can all be the center of fluid cells (case (c)). And if some of those nodes are located in the solid domain, they should be replaced by the corresponding intersection point (case (a) and (b)). Particularly, the Eq. (39) may be substituted by the following Eq. (40) where the normal gradient condition is imposed on those intersection nodes,

$$\frac{\partial\chi(\boldsymbol{x})}{\partial n} = an_x + bn_y + c(xn_y + yn_x), \tag{40}$$

with $\boldsymbol{n} = (n_x, n_y)$. As for the Robin condition, both Eqs. (39) and (40) are involved, and the constrain equation for the four parameters of a, b, c and d should be replaced as

$$m_1(an_x + bn_y + c(xn_y + yn_x)) + m_2(ax + by + cxy + d) = m_3. \tag{41}$$

After the evaluation of the macroscopic quantities and non-equilibrium part according to the GBI method, the distribution functions for both the fluid and temperature fields can be determined by the Eq. (33).

3. Numerical examples

The performance of the GC-DUGKS for simulating the thermal flows with heat flux condition at curved surface will be tested in this section. The heat conduction in an annulus with analytical solution available is first simulated to explore its convergence rate.

Five convection-diffusion problems of the natural convection between two cylinders, mixed convection in a cavity with an insulted circular block, convection flow in enclosure with two rotating insulted cylinders, natural convection in a cavity with an inclined elliptical cylinder, and thermal flow past a cylinder with Robin condition are further simulated. Three criterion numerals of Reynolds, Prandtl and Rayleigh numbers are usually involved in those flows. They are expressed as

$$Re = \frac{UL}{\nu}, \quad Pr = \frac{\nu}{\kappa}, \quad Ra = \frac{g_0 \beta Q L^4}{\nu \kappa^2} or \frac{g_0 \beta \Delta T L^3}{\nu \kappa}, \tag{42}$$

where L and U are respectively the characteristic length and velocity. Note that U is not presented directly in some cases, where it is formulated for the flow with non-adiabatic interface as

$$U = \sqrt{\frac{g_0 \beta Q L^2}{\kappa}}. \tag{43}$$

In Eq. (42), ΔT in the second definition of Ra (which is for the flow with curved adiabatic interface) is the temperature difference between two surfaces with known temperature. Moreover, the Nusselt number is generally defined for evaluating the intensity of convective heat transfer as

$$Nu = -\frac{\frac{\partial T}{\partial \boldsymbol{n}} L}{\Delta T}|_{wall}, \tag{44}$$

where $\boldsymbol{n}$ is the outward unit vector normal to the surface. In the simulations, the incompressible flow assumption holds with the Mach number $Ma = 0.1$; the RT_1 is fixed at 1/3; the time step is determined by the Courant-Friedrichs-Lewy (CFL) number in DUGKS as

$$\Delta t = \frac{CFL}{\sqrt{6RT_1}} \Delta x_{\min}, \tag{45}$$

where Δx_{min} is the minimum spatial step, and CFL is set to be 0.8.

3.1. Heat conduction in an annulus

The convergence rate of the present method for the temperature field is first explored. The test problem is the heat conduction in an annulus [35,36]. As shown in Fig. 2, the radii of the outer and inner cylinders are $R_o = 2$ and $R_i = 1$, respectively. For the temperature, the outer one is fixed at $T_c = 0$, and the inner one has a heat flux boundary condition with $\partial T/\partial \boldsymbol{n} = -1$. In this thermal flow, the gap between the concentric circular cylinders, i.e., $(R_o - R_i) = 1$ is taken as the characteristic length. At steady state, this problem has an analytical solution of the temperature as [35]

$$T(r) = \ln(2) - \ln(r), \tag{46}$$

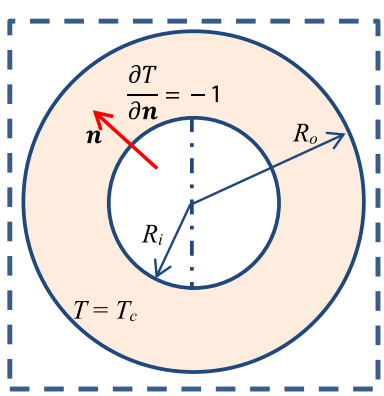

Fig. 2. Schematic of the heat conduction in an annulus. The dashed line denotes the computational domain.

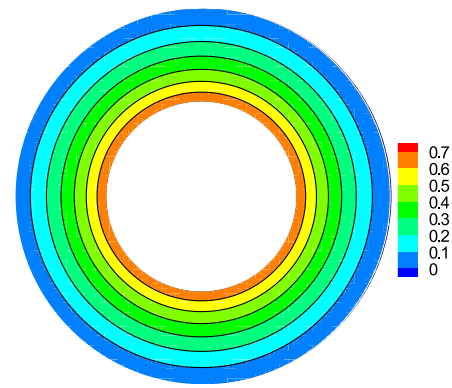

Fig. 3. Isotherms between the two concentric cylinders.

where r ranging from 1 to 2 is the radial distance. We measure the L_2 global relative error,

$$L_2 - error = \sqrt{\sum_{i=1}^{N} (T - T_a)^2 / \sum_{i=1}^{N} (T_a)^2}, \tag{47}$$

where T and T_a are respectively the numerical result by the GC-DUGKS and the analytical solution according to Eq. (46). Since the ghost point for the outer interface is located outside the cylinder, the computational domain should be set to have several more grids than the diameter of the outer cylinder.

Fig. 3 presents the isotherms between the cylinders. The temperature profile is depicted in Fig. 4(a). It is observed that good agreement with the analytical solution is achieved at a coarse mesh of $\Delta x = 1/20$. Fig. 4(b) shows the L_2-*error* of temperature with grid resolutions $\Delta x = 1/15$, 1/20, 1/30 and 1/40. The result indicates that the method is generally second-order accurate in space regarding the temperature field. Note that the diffuse-type IB method was reported previously to achieve only first-order accuracy for this problem by Hu et al. [35] and Suzuki et al. [36].

3.2. Natural convection in an annulus

Simulation of natural convection between two concentric cylinders is performed to validate the present GC-DUGKS for Neumann boundary. The flow condition is illustrated in Fig. 5. As shown in this figure, a small circular cylinder with the heat flux surface of $\partial T/\partial \boldsymbol{n} = -1$ is concentrically embedded in a larger one, which is maintained at a constant low temperature of $T_c = 0$. The two cylinders both keep stationary, and the flow between them is driven by the thermal buoyancy. In the simulations, the radius of the outer cylinder R_o is set at twice to that of the inner one R_i. The flow is subjected to the Prandtl number Pr and Rayleigh number Ra as defined in Eq. (42). The Pr is fixed at 0.7, and two sets of $Ra = 5700$ and 50,000 are considered. The characteristic length $L = (R_o - R_i)$ in this test is resolved by 50 grids. A uniform mesh with 210×210 cells is adopted for the computational domain, which is slightly wider than the diameter of the outer cylinder.

The streamlines and isotherms between the cylinders are depicted in Fig. 6. From this figure, one can find that the flow is symmetric regarding the vertical centerline of the annulus. A couple of crescent-shaped eddies appear between the two cylinders. Meanwhile, the fluid heated by the inner cylinder moves to the upper part of the enclosure. The thermal plume is induced by the convection, which is stronger with the increase of Ra. The patterns of the streamlines and isotherms are the same with those reported in the literature [26,35–38,57]. For quantitative comparison, the distribution of surface temperature for the inner cylinder is further

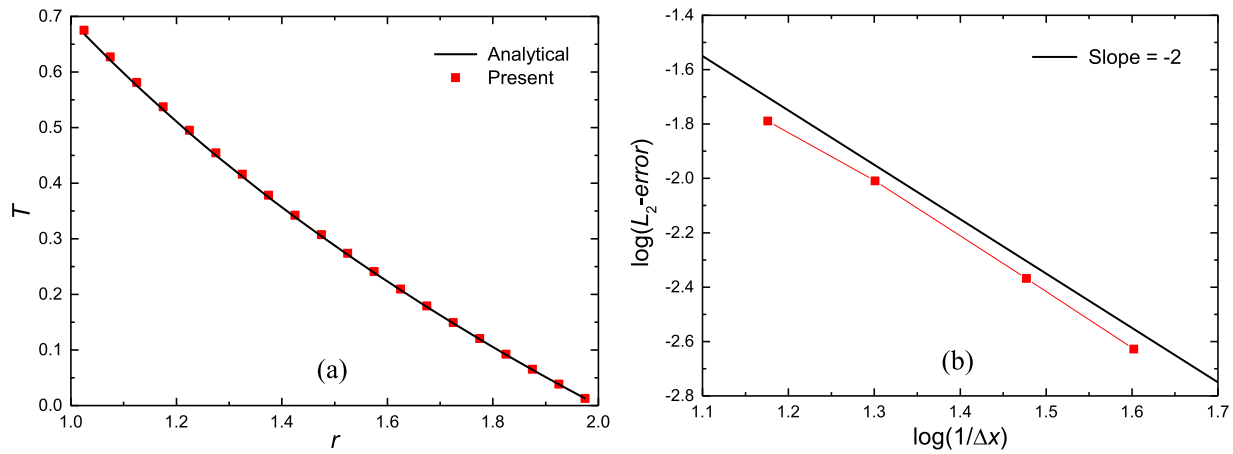

Fig. 4. The temperature profile at mesh $\Delta x = 1/20$ (a) and the L_2-*error* under different grid resolutions (b).

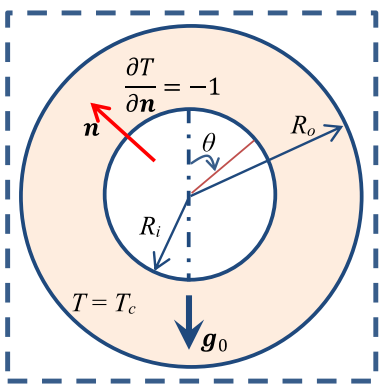

Fig. 5. Geometry arrangement and boundary conditions for the natural convection in an annulus. The dashed line denotes the computational domain.

presented in Fig. 7. The results show a good agreement with the reference data [26,36–38,57].

3.3. Convection flow in a lid-driven cavity with an adiabatic cylinder

In this subsection, the mixed convection is simulated to further test the present GC-DUGKS. The geometry arrangement and boundary conditions are depicted in Fig. 8. A circular block with diameter D is embedded concentrically in a cavity with side length L. The upper surface of the enclosure moves at a constant speed of U_0. The other three straight boundaries are all at rest. For the thermal conditions, the upper wall is hot with temperature T_h, and the bottom wall has a low temperature of T_c; the two vertical boundaries of the enclosure and the cylinder surface are all insulted, i.e., $\partial T/\partial \boldsymbol{n} = 0$. Four non-dimensional parameters of *Pr, Re, Ra* and Richardson number *Ri* are involved in this problem, where the latter is defined as

$$Ri = \frac{Ra}{Re^2 Pr}. \tag{48}$$

It is clear that only three of them are independent. A grid system of 201 × 201 is applied to the cavity. The *Pr* and *Re* are fixed at 0.7 and 100, respectively. The *Ri* ranges from 0.01 to 5 in the simulations.

Fig. 9 illustrates the streamlines and isotherms of this flow at different *Ri*. It can be observed that both patterns are asymmetrical because of the moving upper wall. When the $Ri = 0.01$ is small (Fig. 9(a)), a large eddy appears at the top right corner of the enclosure. It diminishes and moves towards the cylinder surface with

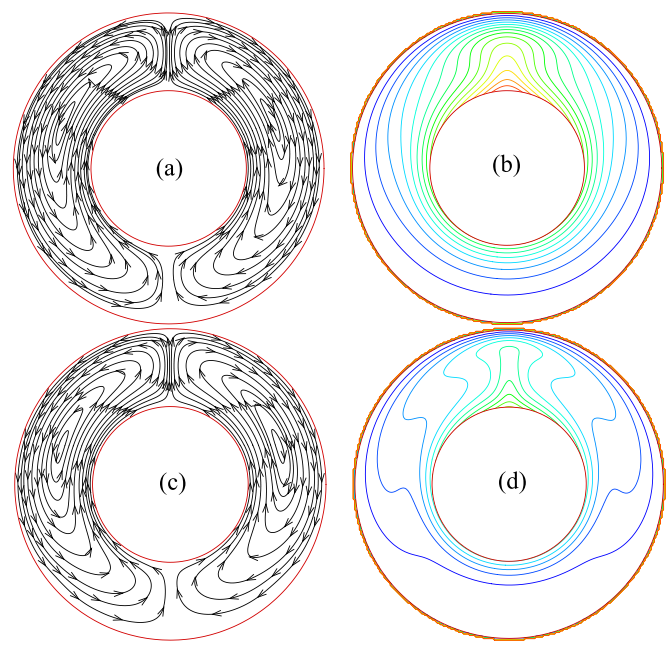

Fig. 6. Streamlines (a,c) and isotherms (b,d) in the annulus at $Ra = 5700$ (a,b) and 50,000 (c,d).

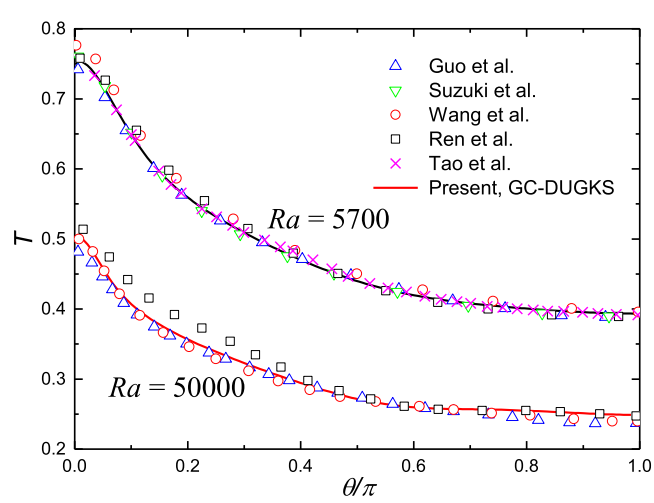

Fig. 7. The surface temperature distribution of the inner cylinder.

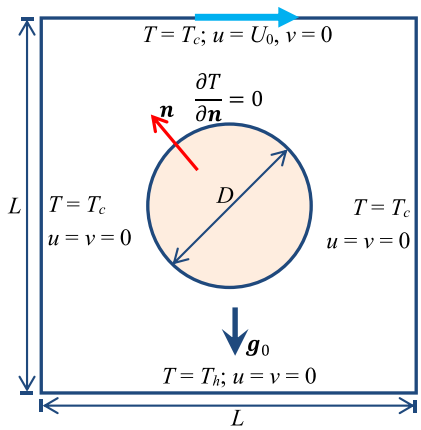

Fig. 8. Geometry arrangement and boundary conditions of the lid-driven flow with an adiabatic block.

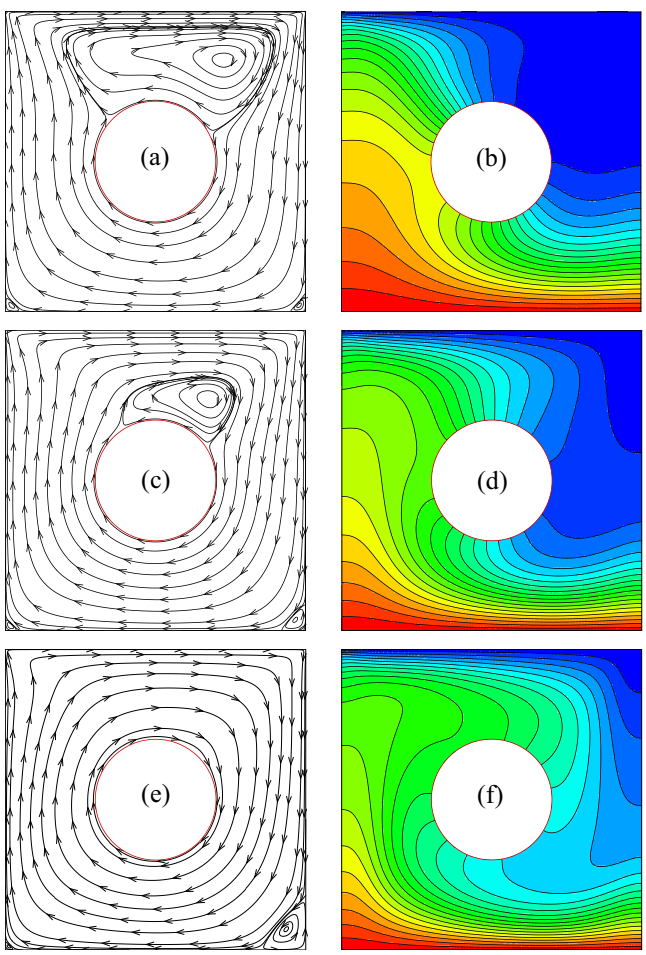

Fig. 9. Streamlines (left) and isotherms (right) in the lid-driven cavity at $Ri = 0.01$ (a,b), 1 (c,d) and 5 (e,f).

Ri increased to 1 (Fig. 9(c)). Eventually, that vortex disappears at $Ri = 5$ (Fig. 9(e)). At the same time, vortexes at the bottom left and right corners of the enclosure gradually decrease and become enlarged, respectively. Note that the vortex at the lower-left corner always has a small size. For the temperature field, the cold region is significantly suppressed with the increase of Ri. Furthermore, the isotherms in all cases are perpendicular to the wall of the cylinder, which is reasonable for accurately enforcing the adiabatic conditions. Figs. 10 and 11 present respectively the Nu distribution on

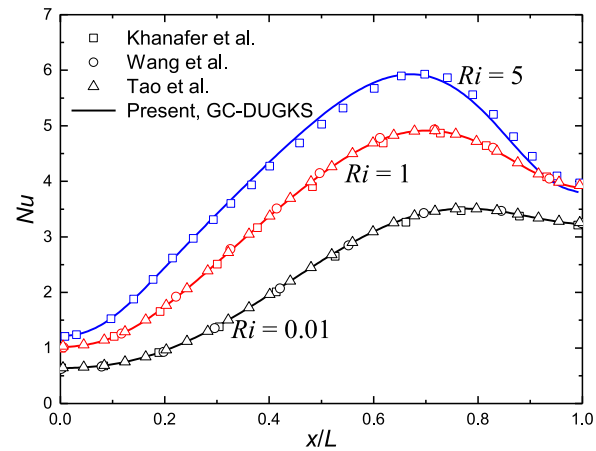

Fig. 10. The Nusselt number distribution on the bottom boundary of the cavity.

the bottom surface of the enclosure, and the temperature distribution along the two profiles of $x/L = 0.15$ and $y/L = 0.15$, together with the reference data by the previous studies [37,39,57]. Those results are generally in consistent with each other.

3.4. Mixed convection in a box with two spinning insulted cylinders

Simulation of the convection flow in an enclosure with two rotating cylinders is carried out in this subsection. The mixed convection in this test case is complex with moving heat-flux surfaces. Fig. 12 depicts the geometry arrangement and boundary conditions. The square box with length L contains two cylinders, which have a diameter of $D = 0.2\ L$. Those cylinders are located along the horizontal centerline of the cavity, both at a distance of 0.25 L regarding the vertical centerline. The four walls of the cavity all keep stationary. For the thermal condition, a temperature difference of $(T_h - T_c)$ exists between the two vertical boundaries, where the left wall is hot with temperature T_h. The horizontal walls of the enclosure and the surface of the cylinders are all adiabatic. Particularly, the left and right cylinders respectively rotate clockwise and counterclockwise at a constant speed of ω.

The streamlines and isotherms in the cavity are presented in Fig. 13. At small $Ri = 0.01$ (Fig. 13(a,b)), both the flow and temperature profiles exhibit certain symmetry regarding the vertical centerline of the cavity. Four vortexes emerge at the cavity corners. The bulk fluid is mainly entrained around the rotating cylinders independently. As the value of Ri increases to 10, the convection dominates the flow in the cavity. The region influenced by the cylinders attenuates dramatically, and more fluid circulates in the entire cavity (Fig. 13(c)). Meanwhile, the temperature filed is obviously asymmetric (Fig. 13(d)). A similar phenomenon had been reported recently by Khanafer et al. [40]. Figs. 14 and 15 further presents the distribution of Nu along the cavity walls, and the temperature profiles at $x/L = 0.5$ and $y/L = 0.5$. The present results match well with reference data in the literature.

3.5. Natural convection in a square box with an inclined elliptical cylinder

We further perform simulation of the convection flow in an enclosure with ellipse shaped obstacle to test the GC-DUGKS for the non-circular boundary. As depicted in Fig. 16, the ellipse with major axis $2r_a = 0.5188\ L$ and minor axis $2r_b = 0.2594\ L$ is placed at the box center, with side length $L = 1$ the characteristic length in this simulation. The inclination angle of the cylinder is $\psi = \pi/4$. The four boundaries of the cavity are cold wall with temperature T_c. The ellipse surface is isothermal with $T = T_h$ or isoflux with

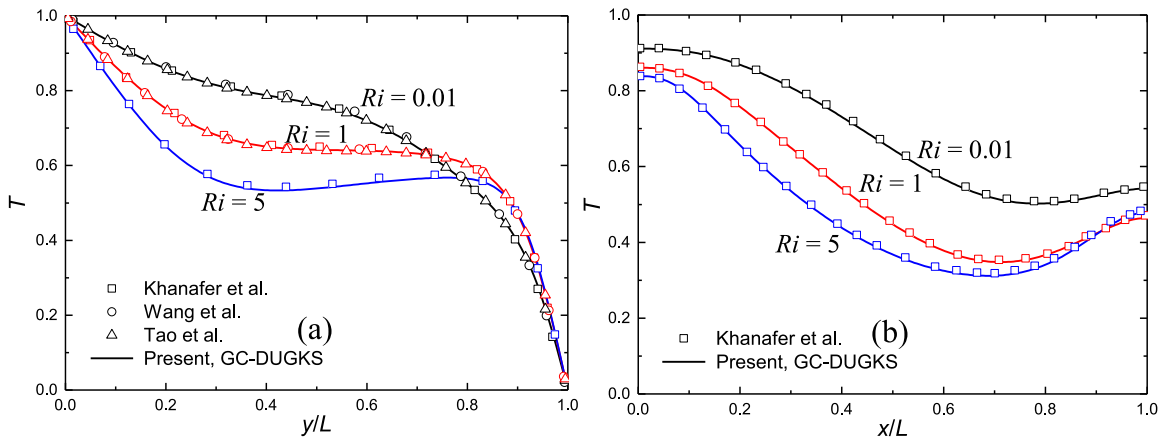

Fig. 11. The temperature distribution along the profiles of $x/L = 0.15$ (a) and $y/L = 0.15$ (b).

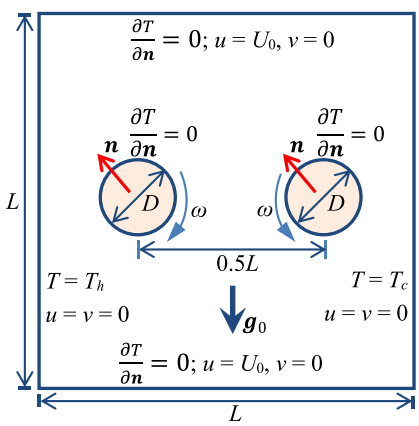

Fig. 12. Geometry configuration and boundary conditions for the mixed convection in an enclosure with two rotating adiabatic cylinders.

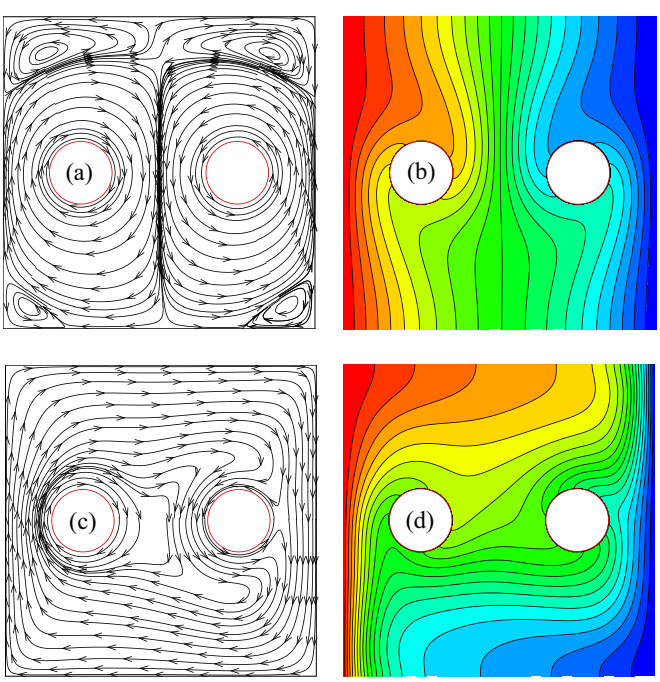

Fig. 13. Streamlines (left) and isotherms (right) in the cavity at $Ri = 0.01$ (a,b) and 10 (c,d).

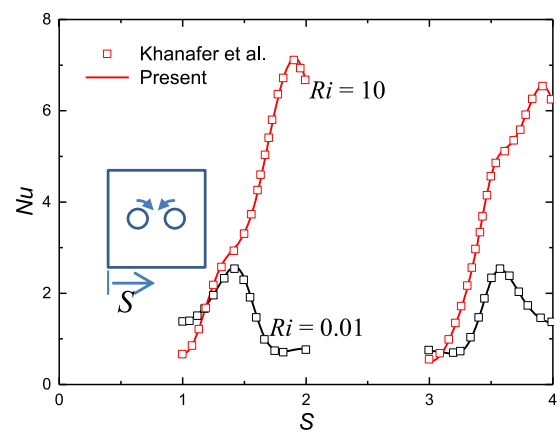

Fig. 14. The anti-clockwise distribution of *Nu* along the cavity walls.

$\partial T/\partial \boldsymbol{n} = -1$. A uniform mesh system of 300 × 300 is applied to the square enclosure. In the simulation, the *Pr* and *Ra* defined by Eq. (42) are fixed at 0.71 and 100,000, respectively.

The streamlines and isotherms in the enclosure with different boundary conditions specified at the elliptical surface are shown in Fig. 17. The inclined ellipse induces the asymmetrical patterns of the streamlines and isotherms. At the isothermal case (Fig. 17(a,b)), a large eddy appears at the upper-left part of the cavity, while two small vortexes are formed between the cylinder and the right wall. Moreover, a strong convection flow is induced by the hot surface of the inner ellipse. On the other hand, the isoflux counterpart exhibits a similar flow pattern (Fig. 17(c)), and at the same time has low convection intensity (Fig. 17(d)). The distribution of the *Nu* along the cavity walls is depicted in Fig. 18. The *Nu* is much smaller at the isoflux case, consistent with the results presented in Fig. 17. The isothermal results match well with the reference data of Liao et al. [50].

3.6. Force convection around a circular cylinder with Robin condition

The above test cases all concern the Neumann boundary condition (i.e., isoflux). In this subsection, the present GC-DUGKS is applied to the thermal flow around a cylinder with Robin condition at the surface, which is a combination of the Dirichlet and Neumann conditions as

$$-\frac{\partial T}{\partial \boldsymbol{n}} + T = 1. \tag{49}$$

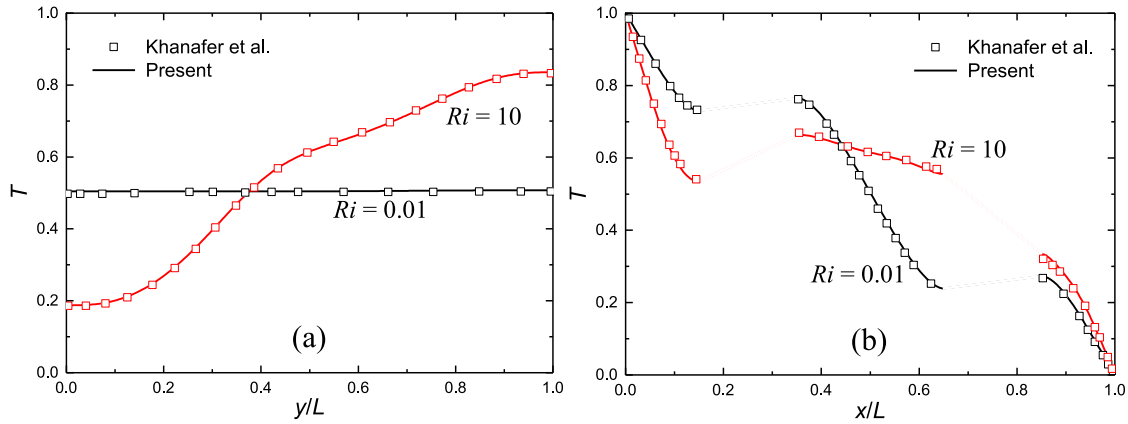

Fig. 15. The temperature distribution along the profiles of $x/L = 0.5$ (a) and $y/L = 0.5$ (b).

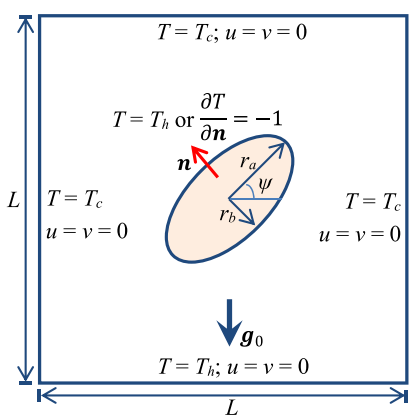

Fig. 16. Schematic of the convection flow in the enclosure with a concentrated elliptical cylinder.

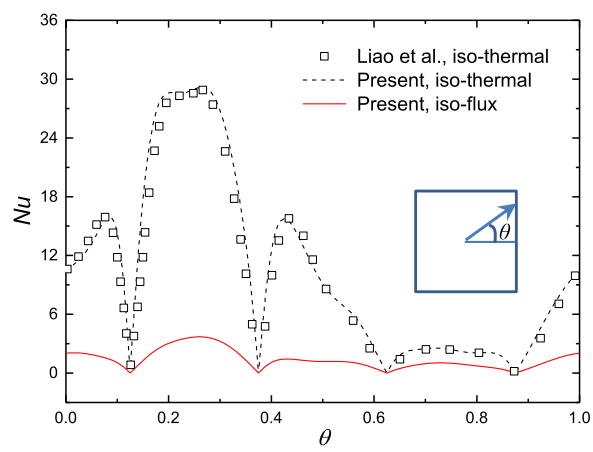

Fig. 18. The anti-clockwise distribution of Nu along the cavity walls at $Ra = 100{,}000$.

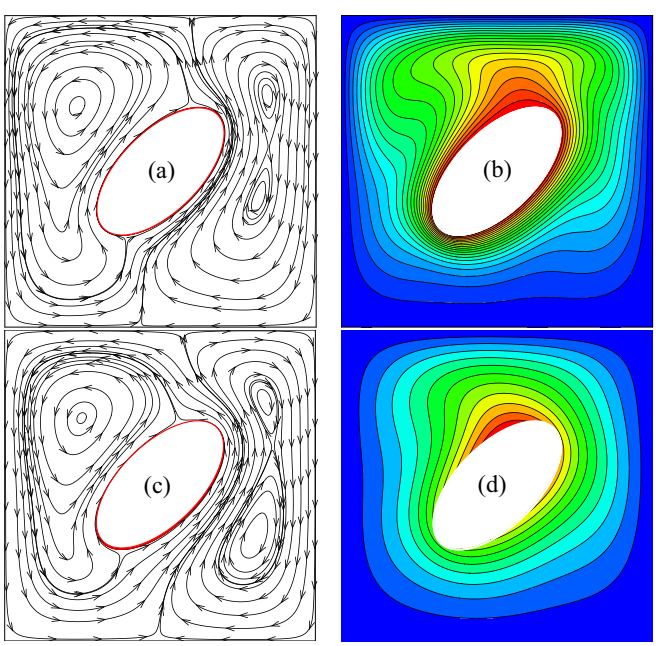

Fig. 17. Streamlines (left) and isotherms (right) in the cavity at $Ra = 100{,}000$. The boundary conditions exerted on the ellipse surface are isothermal (a,b) and isoflux (c,d), respectively.

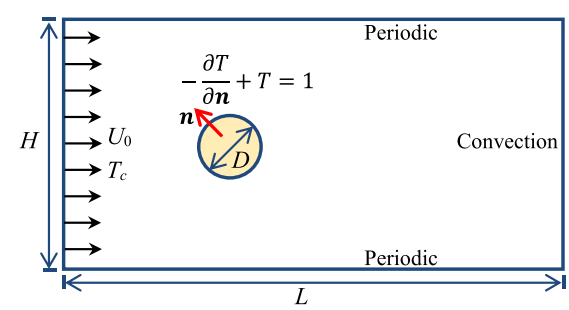

Fig. 19. Geometry configuration and boundary conditions of forced convection around a cylinder with the Robin boundary condition.

As depicted in Fig. 19, the coordinate of a cylinder with diameter $D = 1$ is $(0.25\,L, 0.5H)$, where $L = 40D$ and $H = 20D$ are the length and width of the computational domain. At the inlet, the cold fluid with the temperature T_c moves horizontally at a constant speed of U_0. The Robin condition expressed by Eq. (49) is exerted on the surface of the circular obstacle. Periodic condition is implemented to the horizontal boundaries of the domain. For the outlet, it is specified with the convection boundary condition. Two parameters of the $Re = U_0D/\nu$ and Pr are used to control this flow. In the simulation, they are respectively set to be 20 and 0.71. Furthermore, a non-uniform mesh system of 410×240 with the maximum and minimum spatial steps of $\Delta x_{max} = D/8$ and $\Delta x_{min} = D/40$ respectively (depicted in Fig. 20) is applied to reduce the computational load. It is worth noting that to obtain the

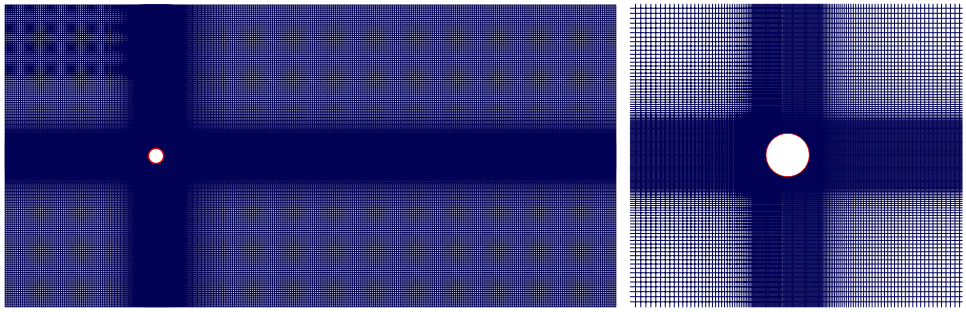

(a) (b)

Fig. 20. The non-uniform mesh used in the simulation (a). (b) is an enlarged view of the mesh around the cylinder.

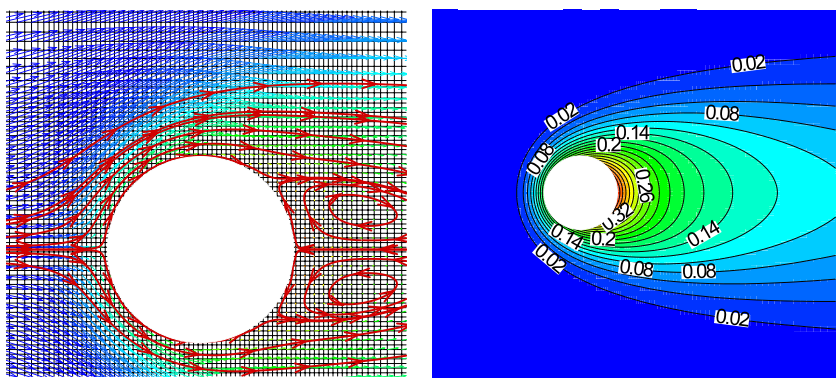

(a) (b)

Fig. 21. Streamlines and velocity vectors (a), and the isotherms (b) around the cylinder at $Re = 20$.

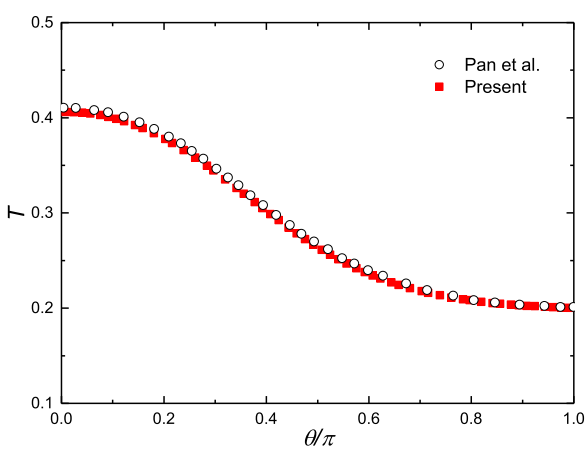

Fig. 22. The temperature distribution on the cylinder boundary at $Re = 20$.

same grid resolution of $\Delta x = D/40$ around the cylinder, the total number of meshes can be up to $1600 \times 800 = 1.28 \times 10^6$ in the uniform mesh system. The non-uniform counterpart is only $410 \times 240 = 9.84 \times 10^4$, which is beneficial to improving the overall computing efficiency.

Fig. 21 displays the streamlines, velocity vectors and isotherms near the circular cylinder. The streamlines, velocity vectors (Fig. 21(a)) and isotherms (Fig. 21(b)) are all smooth around the cylinder, which demonstrates a well implementation of the non-uniform mesh. Meanwhile, as shown in Fig. 21(b), the isotherm is dense (i.e., large temperature gradient) near the front end of the obstacle. Therefore, the convection heat transfer is stronger in the front. The temperature distribution on the obstacle surface is depicted in Fig. 22. As shown in this figure, the cylinder rear and front achieve the maximum and minimum temperatures, respectively. Those results match well with the previous study [49].

4. Conclusions

This study presents the GC-DUGKS method for simulating the thermal convection problems with curved heat-flux condition. The double-population model of DUGKS is adopted to solve the thermal flow, where the two fields of fluid and temperature are coupled using the Boussinesq approximation. The Strang-Splitting method is introduced to incorporate the buoyancy force. As for the curved boundary conditions, they are handled by the ghost cell approach. Particularly, the heat flux boundary is most concerned in the present study, which can be implemented consistently with the hydrodynamic and isothermal conditions.

The heat conduction in an annulus is first simulated to test the convergence rate of the method, where the inner cylinder has a heat flux interface. The result demonstrates a second-order accuracy of the present GC-DUGKS for the temperature field. Simulations of five convection flows with curved heat-flux condition are further carried out to explore the feasibility of the method. Good agreement with the data reported by previously studies is achieved in all those test cases, demonstrating the accuracy and versatility of the method. Since the DUGKS is intrinsically a multi-scale method, we will consider the thermal flows at different regimes in the future work.

Declaration of Competing Interest

We declare no conflicts of interest.

CRediT authorship contribution statement

Shi Tao: Conceptualization, Methodology, Software, Writing - original draft. **Qing He:** Data curation, Writing - review & editing. **Baiman Chen:** Visualization, Investigation. **Frank G.F. Qin:** Formal analysis, Validation. **Yousheng Lin:** Supervision.

Acknowledgments

The authors thank the Editor and referee for their valuable suggestions. This work was supported by the National Natural Science Foundation of China (51906044 and 11902075), the Doctoral Start-up Foundation of Dongguan University of Technology, China (GC300502-39) and the Guangdong Provincial Key Laboratory of Distributed Energy Systems, China (2020B1212060075).

References

[1] Y.L. He, Q. Liu, Q. Li, W.Q. Tao, Lattice Boltzmann methods for single-phase and solid-liquid phase-change heat transfer in porous media: a review, Int. J. Heat Mass Transf. 129 (2019) 160–197.
[2] C. Li, L.P. Wang, An immersed boundary-discrete unified gas kinetic scheme for simulating natural convection involving curved surfaces, Int. J. Heat Mass Transf. 126 (2018) 1059–1070.
[3] C.K. Aidun, J.R. Clausen, Lattice-Boltzmann method for complex flows, Annu. Rev. Fluid Mech. 42 (2010) 439–472.
[4] A. Xu, W. Shyy, T. Zhao, Lattice Boltzmann modeling of transport phenomena in fuel cells and flow batteries, Acta Mech. Sinica 33 (3) (2017) 555–574.
[5] Z. Guo, C. Shu, Lattice Boltzmann Method and Its Applications in Engineering, Vol. 3, World Scientific, 2013.
[6] S. Succi, Lattice boltzmann 2038, EPL (Europhys. Lett.) 109 (5) (2015) 50001.
[7] M.H. Saadat, F. Bösch, I.V. Karlin, Semi-Lagrangian lattice Boltzmann model for compressible flows on unstructured meshes, Phys. Rev. E 101 (2) (2020) 023311.
[8] A. Krämer, D. Wilde, K. Küllmer, D. Reith, H. Foysi, W. Joppich, Lattice Boltzmann simulations on irregular grids: introduction of the NATriuM library, Comput. Math. Appl. (2018).
[9] Z. Guo, K. Xu, R. Wang, Discrete unified gas kinetic scheme for all Knudsen number flows: low-speed isothermal case, Phys. Rev. E 88 (3) (2013) 033305.
[10] Z. Guo, R. Wang, K. Xu, Discrete unified gas kinetic scheme for all Knudsen number flows. II. Thermal compressible case, Phys. Rev. E 91 (3) (2015) 033313.
[11] S. Tao, H.L. Zhang, Z.L. Guo, L.P. Wang, A combined immersed boundary and discrete unified gas kinetic scheme for particle-fluid flows, J. Comput. Phys. 375 (15) (2018) 498–518.
[12] Y. Huo, Z. Rao, The discrete unified gas kinetic scheme for solid-liquid phase change problem, Int. Commun. Heat Mass Transf. 91 (2018) 187–195.
[13] S. Tao, Q. He, L. Wang, S. Huang, B. Chen, A non-iterative direct-forcing immersed boundary method for thermal discrete unified gas kinetic scheme with Dirichlet boundary conditions, Int. J. Heat Mass Transf. 137 (2019) 476–488.
[14] X.P. Luo, H.L. Yi, A discrete unified gas kinetic scheme for phonon Boltzmann transport equation accounting for phonon dispersion and polarization, Int. J. Heat Mass Transf. 114 (2017) 970–980.
[15] J. Shang, Z. Chai, H. Wang, B. Shi, Discrete unified gas kinetic scheme for nonlinear convection-diffusion equations, Phys. Rev. E 101 (2) (2020) 023306.
[16] C.S. Peskin, The immersed boundary method, Acta Numer. 11 (2002) 479–517.
[17] T. Seta, K. Hayashi, A. Tomiyama, Analytical and numerical studies of the boundary slip in the immersed boundary-thermal lattice Boltzmann method, Int. J. Numer. Methods Fluids 86 (7) (2018) 454–490.
[18] Y. Hu, D. Li, S. Shu, X. Niu, Immersed boundary-lattice Boltzmann simulation of natural convection in a square enclosure with a cylinder covered by porous layer, Int. J. Heat Mass Transf. 92 (2016) 1166–1170.
[19] S. Tao, Q. He, J. Chen, B. Chen, G. Yang, Z. Wu, A non-iterative immersed boundary-lattice Boltzmann method with boundary condition enforced for fluid–solid flows, Appl. Math Model 76 (2019) 362–379.
[20] J. Wu, C. Shu, Implicit velocity correction-based immersed boundary-lattice Boltzmann method and its applications, J. Comput. Phys. 228 (6) (2009) 1963–1979.
[21] K. Luo, Z. Wang, J. Fan, K. Cen, Full-scale solutions to particle-laden flows: multidirect forcing and immersed boundary method, Phys. Rev. E 76 (6) (2007) 066709.
[22] M. Jiang, Z. Liu, A boundary thickening-based direct forcing immersed boundary method for fully resolved simulation of particle-laden flows, J. Comput. Phys. 390 (2019) 203–231.
[23] J. Wu, Y. Cheng, L.A. Miller, An iterative source correction based immersed boundary-lattice Boltzmann method for thermal flow simulations, Int. J. Heat Mass Transf. 115 (2017) 450–460.
[24] T. Seta, Implicit temperature-correction-based immersed-boundary thermal lattice Boltzmann method for the simulation of natural convection, Phys. Rev. E 87 (6) (2013) 063304.
[25] Y. Hu, D. Li, S. Shu, X. Niu, An efficient immersed boundary-lattice Boltzmann method for the simulation of thermal flow problems, Commun. Comput. Phys. 20 (5) (2016) 1210–1257.
[26] T. Guo, E. Shen, Z. Lu, Y. Wang, L. Dong, Implicit heat flux correction-based immersed boundary-finite volume method for thermal flows with Neumann boundary conditions, J. Comput. Phys. 386 (2019) 64–83.
[27] Y.H. Tseng, J.H. Ferziger, A ghost-cell immersed boundary method for flow in complex geometry, J. Comput. Phys. 192 (2) (2003) 593–623.
[28] A. Xu, L. Shi, H.D. Xi, Lattice Boltzmann simulations of three-dimensional thermal convective flows at high Rayleigh number, Int. J. Heat Mass Transf. 140 (2019) 359–370.
[29] P. Wang, Y. Zhang, Z. Guo, Numerical study of three-dimensional natural convection in a cubical cavity at high Rayleigh numbers, Int. J Heat Mass Transf. 113 (2017) 217–228.
[30] P.J. Dellar, An interpretation and derivation of the lattice Boltzmann method using Strang splitting, Comput. Math. Appl. 65 (2) (2013) 129–141.
[31] L.M. Yang, C. Shu, J. Wu, Y. Wang, Comparative study of discrete velocity method and high-order lattice Boltzmann method for simulation of rarefied flows, Comput. Fluids 146 (2017) 125–142.
[32] S. Tao, Q. He, B. Chen, X. Yang, S. Huang, One-point second-order curved boundary condition for lattice Boltzmann simulation of suspended particles, Comput. Math. Appl. 76 (7) (2018) 1593–1607.
[33] S. Tao, B. Chen, H. Xiao, S. Huang, Lattice Boltzmann simulation of thermal flows with complex geometry using a single-node curved boundary condition, Int. J. Therm. Sci. 146 (2019) 106112.
[34] A. Tiwari, S.P. Vanka, A ghost fluid Lattice Boltzmann method for complex geometries, Int. J. Numer. Methods Fluids 69 (2) (2012) 481–498.
[35] Y. Hu, D. Li, S. Shu, X. Niu, Study of multiple steady solutions for the 2D natural convection in a concentric horizontal annulus with a constant heat flux wall using immersed boundary-lattice Boltzmann method, Int. J. Heat Mass Transf. 81 (2015) 591–601.
[36] K. Suzuki, T. Kawasaki, N. Furumachi, Y. Tai, M. Yoshino, A thermal immersed boundary–lattice Boltzmann method for moving-boundary flows with Dirichlet and Neumann conditions, Int. J. Heat Mass Transf. 121 (2018) 1099–1117.
[37] Y. Wang, C. Shu, L.M. Yang, Boundary condition-enforced immersed boundary-lattice Boltzmann flux solver for thermal flows with Neumann boundary conditions, J. Comput. Phys. 306 (2016) 237–252.
[38] W. Ren, C. Shu, W. Yang, An efficient immersed boundary method for thermal flow problems with heat flux boundary conditions, Int. J. Heat Mass Transf. 64 (2013) 694–705.
[39] K. Khanafer, S.M. Aithal, Laminar mixed convection flow and heat transfer characteristics in a lid driven cavity with a circular cylinder, Int. J. Heat Mass Transf. 66 (2013) 200–209.
[40] K. Khanafer, S.M. Aithal, K. Vafai, Mixed convection heat transfer in a differentially heated cavity with two rotating cylinders, Int. J. Therm. Sci. 135 (2019) 117–132.
[41] Y. Huo, Z. Rao, The numerical investigation of nanofluid based cylinder battery thermal management using lattice Boltzmann method, Int. J. Heat Mass Transf. 91 (2015) 374–384.
[42] K. Luo, C. Mao, Z. Zhuang, J. Fan, N.E.L. Haugen, A ghost-cell immersed boundary method for the simulations of heat transfer in compressible flows under different boundary conditions Part-II: complex geometries, Int. J. Heat Mass Transf. 104 (2017) 98–111.
[43] P. Wang, L. Zhu, Z. Guo, K. Xu, A comparative study of LBE and DUGKS methods for nearly incompressible flows, Commun. Comput. Phys. 17 (3) (2015) 657–681.
[44] P. Wang, L.P. Wang, Z. Guo, Comparison of the lattice Boltzmann equation and discrete unified gas-kinetic scheme methods for direct numerical simulation of decaying turbulent flows, Phys. Rev. E 94 (4) (2016) 043304.
[45] L. Zhu, P. Wang, Z. Guo, Performance evaluation of the general characteristics based off-lattice Boltzmann scheme and DUGKS for low speed continuum flows, J. Comput. Phys. 333 (2017) 227–246.
[46] C. Shu, Y. Wang, C.J. Teo, J. Wu, Development of lattice Boltzmann flux solver for simulation of incompressible flows, Adv. Appl. Math Mech. 6 (4) (2014) 436–460.
[47] Y. Wang, C. Shu, C.J. Teo, Thermal lattice Boltzmann flux solver and its application for simulation of incompressible thermal flows, Comput. Fluids 94 (2014) 98–111.
[48] L.M. Yang, C. Shu, W.M. Yang, J. Wu, Simulation of conjugate heat transfer problems by lattice Boltzmann flux solver, Int. J. Heat Mass Transf. 137 (2019) 895–907.
[49] D. Pan, A general boundary condition treatment in immersed boundary methods for incompressible Navier-Stokes equations with heat transfer, Numer. Heat Transf., Part B 61 (4) (2012) 279–297.
[50] C.C. Liao, C.A. Lin, Influences of a confined elliptic cylinder at different aspect ratios and inclinations on the laminar natural and mixed convection flows, Int. J. Heat Mass Transf. 55 (23–24) (2012) 6638–6650.
[51] A. Dadone, B. Grossman, Surface boundary conditions for the numerical solution of the Euler equations, AIAA J. 32 (2) (1994) 285–293.
[52] H. Forrer, R. Jeltsch, A higher-order boundary treatment for Cartesian-grid methods, J. Comput. Phys. 140 (2) (1998) 259–277.
[53] M. Mozafari-Shamsi, M. Sefid, G. Imani, Developing a ghost fluid lattice Boltzmann method for simulation of thermal Dirichlet and Neumann conditions at curved boundaries, Numer. Heat Transf., Part B 70 (3) (2016) 251–266.

[54] A. Xu, L. Shi, T.S. Zhao, Accelerated lattice Boltzmann simulation using GPU and OpenACC with data management, Int. J. Heat Mass Transf. 109 (2017) 577–588.
[55] Z. Guo, C. Zheng, B. Shi, Non-equilibrium extrapolation method for velocity and pressure boundary conditions in the lattice Boltzmann method, Chin. Phys. 11 (4) (2002) 366.
[56] S. Chen, D. Martinez, R. Mei, On boundary conditions in lattice Boltzmann methods, Phys. Fluids 8 (9) (1996) 2527–2536.
[57] S. Tao, A. Xu, Q. He, B. Chen, F.G. Qin, A curved lattice Boltzmann boundary scheme for thermal convective flows with Neumann boundary condition, Int. J. Heat Mass Transf. 150 (2020) 119345.